Quantitative explanation of the difference in AC magnetization curves between suspended and immobilized magnetic nanoparticles for biomedical application

Enpuku, Keiji
Department of Electrical and Electronic Engineering, Kyushu University

Yamamura, Shuya
Department of Electrical and Electronic Engineering, Kyushu University

Yoshida, Takashi
Department of Electrical and Electronic Engineering, Kyushu University

出版情報：Journal of Magnetism and Magnetic Materials. 564 (1), pp.170089-, 2022-12-15. Elsevier
バージョン：
権利関係：

Quantitative explanation of the difference in AC magnetization curves between suspended and immobilized magnetic nanoparticles for biomedical application

Keiji Enpuku*, Shuya Yamamura, and Takashi Yoshida

Department of Electrical and Electronic Engineering, Kyushu University, Fukuoka 819-0395, Japan

Abstract

We study the difference in AC magnetization (M–H) curves between suspended and immobilized magnetic nanoparticles (MNPs). We use three commercial MNP samples that are often used for biomedical application. First, we measure the hysteresis area of the AC M–H curve, A, when the amplitude of the excitation field, H_{ac}, is changed. The A vs. H_{ac} curve is compared with previously obtained analytical results by taking account of the MNP size distribution in the sample. We show that they quantitatively agree for both suspended and immobilized samples. From the comparison, we clarify the mechanism that determines the AC M–H curve of a suspended sample. For high H_{ac}, the Néel relaxation becomes dominant in the suspended sample, and alignment of easy axes caused by the AC field increases the hysteresis loss compared to the immobilized case. The effect of Brownian relaxation in the suspended sample increases with decreasing H_{ac} and gives additional loss at low field. The portion of Néel-relaxation- and Brownian-relaxation-dominant MNPs in the sample is quantitatively evaluated. We also clarify the difference in harmonic signals between suspended and immobilized samples. Finally, we discuss the condition for the MNP parameters and excitation field that determines the dominant relaxation mechanism in a suspended sample.

Key words

Magnetic nanoparticle; Néel relaxation; Brownian relaxation; hysteresis loss; harmonic signals; easy axis alignment

1. Introduction

The AC magnetization (*M–H*) curve of magnetic nanoparticles (MNPs) has been widely studied for biomedical application. For example, MNP hysteresis loss has been studied for magnetic hyperthermia, where the loss is used to raise the temperature of cancer cells to kill them [1-9]. Harmonic signals caused by nonlinear magnetization have been studied for magnetic particle imaging (MPI), where the three-dimensional position of MNPs is detected with high temporal resolution for medical diagnosis [10-13]. Harmonic signals are also used for magnetic biosensing, where disease-related biological targets are detected using bio-functionalized MNPs [14-18].

These magnetic properties are different between suspended and immobilized MNPs. The difference in these properties can also be used to magnetically distinguish the suspended and immobilized MNPs when they coexist in a sample. For immobilized MNPs, the dynamic behavior is determined by Néel relaxation. The easy axis of magnetization is fixed regardless of time, and only the magnetic moment vector rotates owing to Néel relaxation when an AC field is applied. However, for MNPs suspended in liquid, both the Brownian and Néel relaxations affect the AC *M–H* curve. Both the easy axis and magnetic moment vector rotate owing to Brownian and Néel relaxation, respectively.

The extent to which Brownian or Néel relaxation contributes to the AC *M–H* curve of suspended MNPs considerably depends on MNP parameters and excitation conditions. As a result, the AC *M–H* curve of suspended MNPs becomes very complicated. Thus far, theoretical studies have been done for two limiting cases. One is $\tau_N(H) >> \tau_B(H)$, where $\tau_N(H)$ and $\tau_B(H)$ are the field-dependent Néel and Brownian relaxation times, respectively. In this case, the AC *M–H* curve of suspended MNPs is determined by linear or nonlinear Brownian relaxation [4, 19]. The other case is $\tau_N(H) << \tau_B(H)$. In this case, the dynamic behavior of suspended MNPs is primarily dominated by Néel relaxation. The magnetic moment rotation is caused by Néel relaxation. In addition, when the field *H* becomes strong, successive Brownian (or physical) rotation of suspended MNPs occurs, causing partial alignment of easy axes [20-25]. We note that the mechanism that gives the difference in AC *M–H* curves between suspended and immobilized MNPs is different for the two cases.

The condition under which these two cases can be applied is determined not only by the MNP parameters but also by the amplitude and frequency of the excitation field *H*. This is because τ_B and τ_N depend on *H*. As a result, *H* determines whether MNP behavior is Néel-relaxation-dominant or Brownian-relaxation-dominant even when MNP parameters are fixed. Therefore, it is necessary to quantitatively clarify the condition for each of these two cases in a suspended sample. When this condition is obtained, we can clarify the mechanism that results in the different AC *M–H* curves between suspended and immobilized MNPs.

In this paper, we study the difference in the AC *M–H* curves between suspended and immobilized MNPs. We use three commercial MNP samples that are often used for biomedical application. First, we evaluate the magnetic parameters such as the saturation magnetization, M_s, anisotropy constant, *K*

and distribution of magnetic core size d_c in each sample. Next, the hysteresis area of the AC *M–H* curve, *A*, is measured when the amplitude of the excitation field, H_{ac}, is changed. The measured *A* vs. H_{ac} curve is compared with analytical results. We show quantitative agreement between them for both suspended and immobilized samples. From the comparison, we clarify how the Brownian and Néel relaxations contribute to the hysteresis loss in a suspended sample. For our samples, easy axis alignment caused by the AC field increases the loss at high fields, while Brownian relaxation increases the loss at low fields. We also show the difference in harmonic signals between suspended and immobilized samples. Finally, we discuss the condition for the MNP parameters and excitation field that determines the dominant relaxation in a suspended sample.

2. Materials and methods

We used three commercial MNP samples: synomag (micromod GmbH, Germany), MS1 (Meito, Japan) and perimag (micromod GmbH, Germany), hereafter denoted as SY, MS and PE, respectively. The samples are multi-core based magnetic nanoparticles, and consist of elementally particles and crystallized agglomerates of elementary particles. We emphasize that the agglomerates are crystallized and can thus be regarded as an effective single core with size d_c, as discussed in previous papers [26, 27].

Synomag consists of maghemite (γ-Fe_2O_3) cores covered by a dextran shell, and their hydrodynamic diameter is nominally d_H = 50 nm [28]. *Riahi et al* presented a transmission electron microscope (TEM) image of synomag, and obtained physical size of particles as d_{TEM} = 9 and 24.3 nm for elementary particles and agglomerates, respectively [29]. They also obtained d_H = 66.5 nm using the dynamic light scattering (DLS) measurement. MS1 are carboxydextran-coated nanoparticles of a mixture of magnetite (Fe_3O_4) and maghemite, and are magnetically fractionated from Resovist (FUJIFILM RI Pharma, Japan) so as to have large core size [30]. The values of d_H = 55.2 nm and d_{TEM} = 4.6 nm for elementary particles were reported for Resovist in ref. [29], but the d_{TEM} value for agglomerates was unknown. Perimag consists of maghemite cores covered by a dextran shell with d_H = 130 nm [28]. *Tay et al* obtained d_{TEM} = 5.5 nm for elementary particles of perimag [31], but the d_{TEM} value for agglomerates was not reported.

We first measured the DC *M–H* curve of each sample suspended in water up to $\mu_0 H_{dc}$ = 1 T using a homemade measurement system based on vibrating sample magnetometer (VSM) method. The distribution of d_c was estimated by analyzing the DC *M–H* curve.

Then, the AC *M–H* curves were measured for both the suspended and immobilized samples. For the suspended sample, 150 μg-Fe of MNPs were dispersed in 150 μL of water. For the immobilized sample, 150 μg-Fe of MNPs were dispersed in 150 μL of epoxy resin. The epoxy resin was initially liquid and began to solidify after 10 min, and almost completely solidified in about 1 h. When the epoxy resin is in liquid state, Brownian rotation of MNPs occurs, and the easy axes of MNPs become

randomly oriented. Then, solidification of the epoxy resin occurs. Therefore, MNPs are immobilized with randomly oriented easy axes when solidification of the epoxy resin completes [24].

The AC *M–H* curves were measured using a homemade measurement system, whose details were mentioned in our previous paper [32]. The excitation field frequency was f = 20 kHz, and the amplitude was changed from $\mu_0 H_{ac}$ = 8 to 20 mT.

3. Results

3.1. Evaluation of MNP parameters

In the present paper, we assume that M_s and K are constant in sample, i.e., they are independent of core size d_c. Table I lists the parameters of the three MNP samples, obtained as follows. First, we measured the DC magnetization (M_{dc}-H_{dc}) curve. The M_{dc} value was almost saturated at $\mu_0 H_{dc}$ = 1 T. For simplicity, therefore, M_s was obtained from M_{dc} measured at $\mu_0 H_{dc}$ = 1 T. We obtained M_s = 345, 360 and 295 kA/m for synomag, MS1 and perimag, respectively. We note that the linear relationship between M_{dc} and $1/H_{dc}$ was observed at high fields $\mu_0 H_{dc} > 0.3$ T, as expected from the Langevin function (see Eq. (A3) in Appendix A). The M_s value can also be estimated by extrapolating the linear M_{dc} vs $1/H_{dc}$ relation to $1/H_{dc} = 0$ [33], and we obtained M_s = 348, 366 and 298 kA/m for synomag, MS1 and perimag, respectively. These values were almost the same as the M_s values obtained from M_{dc} measured at $\mu_0 H_{dc}$ = 1 T.

The distribution of the core size d_c in an MNP sample was obtained by analyzing the measured M_{dc}–H_{dc} curve [34] (see Appendix A). The distribution was expressed as a d_c vs. $n(d_c)V_c$ curve, where $n(d_c)$ is the number density of MNPs with a core diameter d_c per unit of MNP volume, and $V_c = (\pi/6)d_c^3$ is the volume of the magnetic core. Fig. 1 presents the results for the three samples. The d_c vs. $n(d_c)V_c$ curve has two peaks for all three samples. The peak at small d_c (near d_c = 6 nm) corresponds to elementary particles, while the peak at large d_c corresponds to crystallized agglomerates. The portion of agglomerates is much larger than that of elementary particles. The agglomerate d_c value is distributed from 12 to 30 nm for synomag. For MS1 and perimag, d_c for the agglomerates ranged from 10 to 45 nm. The typical agglomerate d_c value, $d_{c,typ}$, that gives the peak of $n(d_c)V_c$ is $d_{c,typ}$ = 17.8, 23.7 and 24.6 nm for synomag, MS1 and perimag, respectively.

Table I. Parameters of the three MNP samples

sample	M_s (kA/m)	K (kJ/m^3)	$\mu_0 H_k$ (mT)	$d_{c,typ}$ (nm)	m_{typ} (10^{-18} Am^2)	σ_{typ}
synomag	345	9.7	56.2	17.8	1.02	6.9
MS1	360	7.0	38.9	23.7	2.51	11.8
perimag	295	5.8	39.3	24.6	2.30	10.9

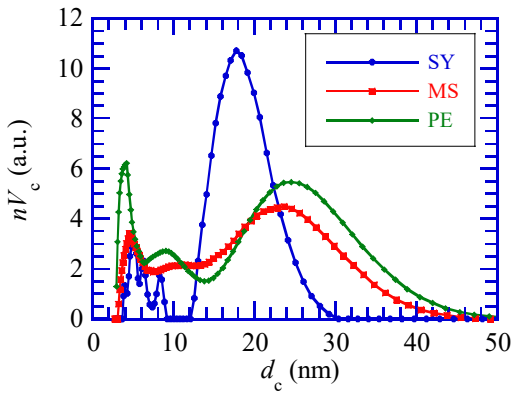

Fig. 1. Core size distribution for the three MNP samples: synomag (SY), MS1 (MS) and perimag (PE).

Examples of the AC *M–H* curves are shown in Fig. 2(a). They were measured for immobilized (solid) and suspended (water) MS1 samples when f = 20 kHz and $\mu_0 H_{ac}$ = 20 mT. The M value and hysteresis of the suspended sample were larger than those of the immobilized sample.

The anisotropy constant K was estimated by analyzing the coercive field $\langle H_c \rangle$ of the AC *M–H* curve for the immobilized sample. An analytical expression for $\langle H_c \rangle$ accounting for the d_c distribution has been obtained in ref. [35] [Eq. (B4) in Appendix B]. This expression was compared with the measured $\langle H_c \rangle$– H_{ac} curve taking K as an adjustable parameter. The value of K was determined to obtain the best fit between experiment and analysis. Fig. 2(b) presents the $\langle H_c \rangle$– H_{ac} curve obtained for the three samples. Symbols represent the experimental results, while the solid lines are the analytical results. The value of K was chosen as 9.7, 7.0 and 5.8 kJ/m^3 for synomag, MS1 and perimag, respectively. We obtained good agreement between analysis and experiment for synomag. For MS1 and perimag, agreement was good at high fields, but deviation occurred at low fields. We note that the K values obtained for synomag and MS1 were a little larger than those reported in ref. [35]. This will be because magnetic parameters are slightly different for each product lot.

From M_s and K, the field H_k is defined as

$$H_k = \frac{2K}{\mu_0 M_s}. \quad (1)$$

Synomag has highest H_k, while MS1 and perimag have similar H_k values, as shown in Table I.

Using the $d_{c,typ}$ values in Table I, we also estimated the typical values of m_{typ}=$M_s V_{c,typ}$ and σ_{typ} = $KV_{c,typ}/(k_B T)$, where k_B is the Boltzmann constant and T is the absolute temperature. These values increase in the order synomag, perimag and MS1, as shown in Table I.

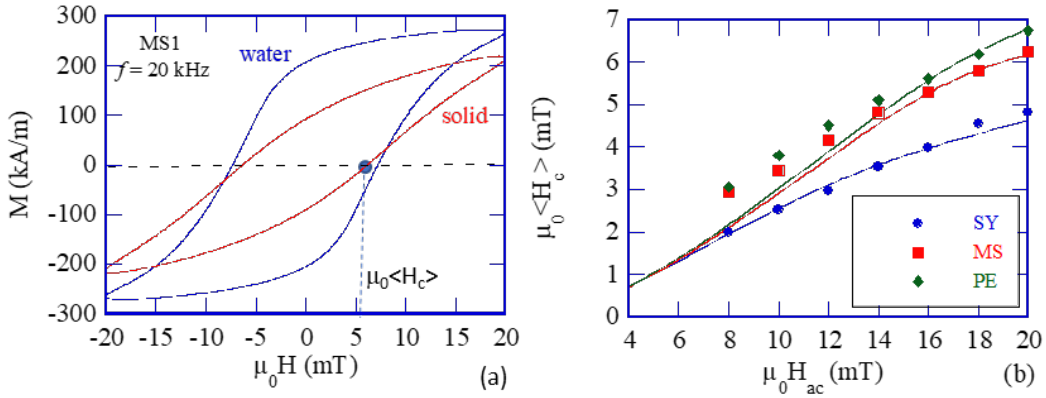

Fig. 2. (a) AC *M*–*H* curve of the MS1 sample measured at f = 20 kHz and $\mu_0 H_{ac}$ = 20 mT. (b) $\langle H_c \rangle$–H_{ac} curves for the three immobilized MNP samples. Symbols are experimental results, while the solid lines are analytical results obtained from Eq. (B4). The calculation used the values K = 9.7, 7.0 and 5.8 kJ/m^3 for synomag, MS1 and perimag, respectively.

3.2. Hysteresis loss

We consider the case when the AC excitation field

$$H(t) = H_{ac} \sin(2\pi f t) \quad (2)$$

is applied to an MNP sample. The hysteresis loss per unit cycle, $\langle A \rangle$, is given by

$$\langle A \rangle = -\oint \mu_0 \boldsymbol{M} \cdot d\boldsymbol{H} = \pi \mu_0 H_{ac} \mathrm{Im}[M_1], \qquad (3)$$

where Im[M_1] is the imaginary part of the fundamental component M_1 when $M(t)$ is expressed as a Fourier series. We obtained Im[M_1] from the measured $M(t)$, and then obtained $\langle A \rangle$ using Eq. (3).

3.2.1. Immobilized MNPs with randomly oriented easy axes

We first study $\langle A \rangle$ for an immobilized MNP sample, where the AC *M*–*H* curve is determined by Néel relaxation. Fig. 3 shows the dependence of $\langle A \rangle$ on H_{ac}. Red circles represent the measured $\langle A \rangle$ vs. H_{ac} curves for immobilized (solid) MNP samples. The results for synomag, MS1 and perimag are shown in Fig. 3(a), 3(b) and 3(c), respectively.

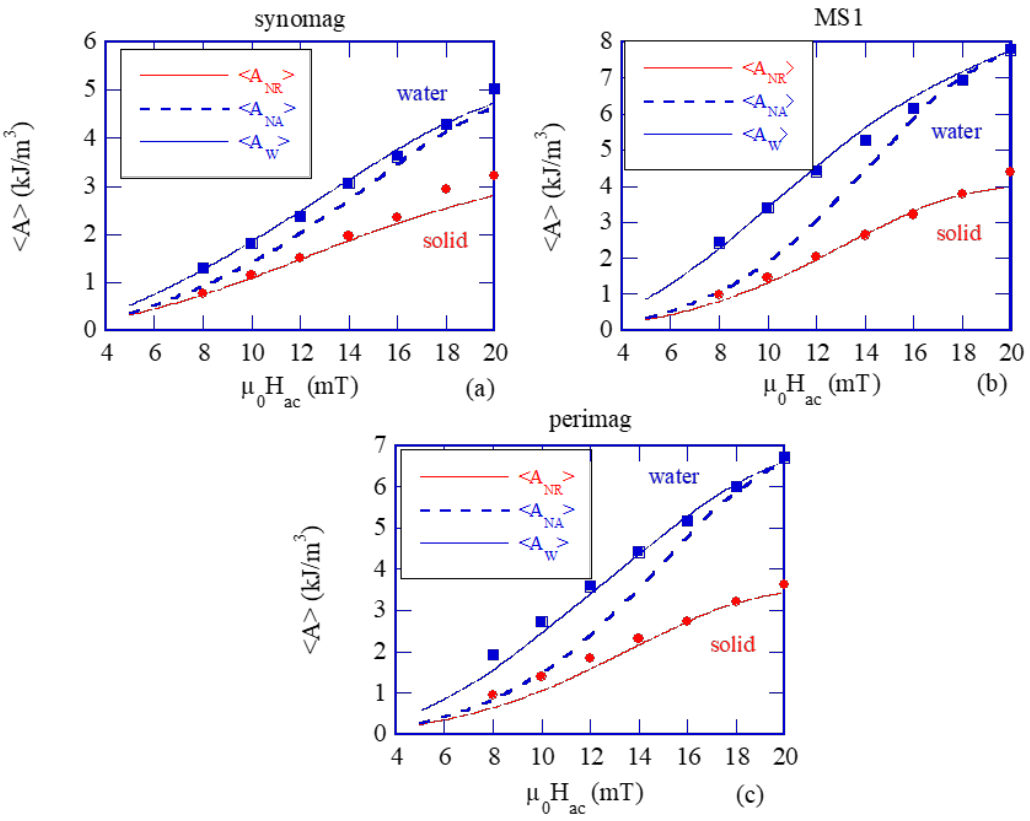

Fig. 3. <*A*> vs. H_{ac} curve for (a) synomag, (b) MS1 and (c) perimag. Circles and rectangles represent the experimental results for the immobilized (solid) and suspended (water) samples, respectively. The lines are calculated from Eqs. (11) and (19).

We compare these experimental results with analysis. When MNPs have the same core size d_c and their easy axes are randomly oriented, an empirical expression for A, which we denote as A_{NR}, was obtained based on numerical simulation, and is given by [36]

$$A_{NR}(d_c) = \begin{cases} 1.92K(1-1.08\kappa) \times g_{NR} \text{ for } \kappa < 0.63 \\ 1.92K\exp\left\{-\left(\dfrac{\kappa}{0.6}\right)^{2.2}\right\} \times g_{NR} \text{ for } \kappa > 0.63, \end{cases} \quad (4)$$

with

$$\kappa = \frac{1}{\sigma}\ln\left(\frac{1}{4\xi_{ac} f \tau_0}\right), \quad (5)$$

where $\sigma = KV_c/(k_BT)$, $\xi_{ac} = \mu_0 m H_{ac}/(k_BT)$ and $m = M_sV_c$ is the magnetic moment. τ_0 is the characteristic time and was set as $\tau_0 = 10^{-9}$ s.

The value of g_{NR} in Eq. (4) is given by

$$g_{NR} = \frac{\exp\left(\frac{h_{ac} - h_1}{\Delta h}\right)}{1 + \exp\left(\frac{h_{ac} - h_1}{\Delta h}\right)}, \qquad (6)$$

with

$$h_1 = 0.12\left(h_{ac,th}\right)^2 + 0.72h_{ac,th} + 0.06, \qquad (7)$$

$$h_{ac,th} = \begin{cases} 0 & \text{for } \sigma \le \sigma_{th}, \\ 0.6\left(1 - \frac{\sigma_{th}}{\sigma}\right) & \text{for } \sigma > \sigma_{th} \end{cases} \quad (8)$$

$$\Delta h = 0.025\,, \quad (9)$$

where $h_{ac} = H_{ac}/H_k$ is the normalized field amplitude. The value of σ_{th} in Eq. (8) is determined by the frequency f of the applied field that satisfies the condition

$$2\pi f \tau_N(0) = \frac{\pi^{\frac{3}{2}}}{\sqrt{\sigma_{th}}} f\tau_0 \exp(\sigma_{th}) = 1. \quad (10)$$

When d_c is distributed in the sample, the hysteresis loss of the sample, $\langle A_{NR} \rangle$, is given by

$$\langle A_{NR} \rangle = \frac{1}{\int_0^\infty nV_c\, dd_c} \int_0^\infty nV_c\, A_{NR}(d_c) dd_c. \quad (11)$$

The red lines in Fig. 3 represent $\langle A_{NR} \rangle$ calculated with Eq. (11) for the three samples. In the calculation, the value of nV_c was obtained from the d_c vs. $n(d_c)V_c$ curve in Fig. 1. The values of M_s, K and H_k in Table I were used, and the value of σ_{th} was obtained from Eq. (10) as σ_{th}=10.3 for f = 20 kHz. As shown in Fig. 3, we obtained good agreement between experiment and analysis for the three MNP samples, indicating the validity of Eq. (11). We emphasize that there is no adjustable parameter in the calculation.

3.2.2. Suspended MNPs

Next, we study $\langle A \rangle$ for MNP samples suspended in water. In Fig. 3, blue rectangles represent the measured $\langle A \rangle$ vs. H_{ac} curve for suspended (water) MNP samples. As shown, $\langle A \rangle$ for the water sample was much larger than for the solid sample.

We compare these experimental results with analysis. For suspended MNPs, analytical expressions for hysteresis loss were obtained for two limiting cases, as shown below.

3.2.2.1. Hysteresis Loss due to Brownian relaxation

An analytical expression for Im[M_1] in Eq. (3) has been obtained for the dynamics of suspended MNPs dominated by Brownian relaxation [19]. The hysteresis loss in this case, A_{BR}, is given by

$$A_{BR}(d_c, d_H) = \frac{\pi\mu_0 H_{ac} M_s}{3} \xi_{ac} k''(\xi_{ac}) g_{BR}(\xi_{ac}) \frac{2\pi f \tau_B(H)}{1 + [2\pi f \tau_B(H)]^2} \quad (12)$$

with

$$k''(\xi_{ac}) = 1 + \frac{0.024\xi_{ac}^2}{1 + 0.18\xi_{ac} + 0.033\xi_{ac}^2}\,, (13)$$

$$g_{BR}(\xi_{ac}) = 1 - \frac{\xi_{ac}^3}{10 + 9\xi_{ac} + 3.81\xi_{ac}^2 + \xi_{ac}^3}\,. (14)$$

The quantity $\tau_B(H)$ in Eq. (12) is the field-dependent Brownian relaxation time given by [19, 37]

$$\tau_B(H) = \frac{\tau_{B,0}}{\sqrt{1 + 0.07\xi_{ac}^2}}\,, (15)$$

where $\tau_{B,0} = 3\eta V_H/(k_B T)$, η is the liquid viscosity (0.86 mPa s for water), and d_H and $V_H = (\pi/6)d_H^3$ are the hydrodynamic diameter and hydrodynamic volume of an MNP, respectively.

3.2.2.2. Hysteresis loss due to Neel relaxation with easy axis alignment

We consider the case $\tau_N(H) < 1/(2\pi ft) << \tau_B(H)$, where the MNP dynamics is primary dominated by Néel relaxation. In addition, the AC field causes successive Brownian (physical) rotation of suspended MNPs, and the easy axes are partially aligned along the applied field [20, 25]. The empirical expression for A in this case, A_{NA}, is [38]

$$A_{NA} = A_{NR} \times R_A\,, (16)$$

where A_{NR} is the hysteresis loss when MNPs are immobilized with randomly oriented easy axes and is given in Eq. (4). R_A represents the increase in loss due to easy axis alignment and is given by

$$R_A = 1 + 1.2\tanh\big(0.12\xi_{eff}\big), \xi_{eff} = \frac{k_{eff}}{\sqrt{2}}\xi_{ac}\,, \qquad (17)$$

$$k_{eff} = \begin{cases} \dfrac{h_{ac}}{1.15\big(1-\sqrt{\kappa}\big)}[0.28 + 0.009(\sigma\kappa)^2] \text{ for } h_{ac} < 1.15\big(1-\sqrt{\kappa}\big) \\ 0.28 + 0.009(\sigma\kappa)^2 \text{ for } h_{ac} \geq 1.15\big(1-\sqrt{\kappa}\big)\,, \end{cases} \qquad (18)$$

where $k_{eff} = 0$ for $\kappa > 1$, and $k_{eff} = 1$ when the right side of Eq. (18) is greater than 1.

3.2.2.3. Hysteresis loss for a suspended MNP sample

We combine A_{BR} in Eq. (12) and A_{NA} in Eq. (16) to obtain the hysteresis loss for the suspended sample, $\langle A_W \rangle$. As shown in Fig. 4, A_{NA} becomes dominant for smaller d_c, while A_{BR} becomes dominant for larger d_c. We obtain the following approximate expression for $\langle A_w \rangle$ when d_c is distributed in the sample:

$$\langle A_w \rangle = \frac{1}{\int_0^\infty nV_c\, dd_c}\left\{\int_0^{d_{c,B}} nV_c\, A_{NA}(d_c)dd_c + \int_{d_{c,B}}^\infty nV_c\, A_{BR}(d_c)dd_c\right\}, \qquad (19)$$

where $d_{c,B}$ is the value of d_c that distinguishes the two cases.

An example of the d_c vs. nV_cA curve is shown in Fig. 4. The blue and red lines show the d_c vs.

nV_cA_{NA} and d_c vs. nV_cA_{BR} curves, respectively. These curves are calculated for the MS1 sample with d_H = 60 nm when f = 20 kH and $\mu_0 H_{ac}$ = 14 mT. We obtained $d_{c,B}$= 31 nm for this case. In Eq. (19), therefore, we use A_{NA} for $d_c < d_{c,B}$ and A_{BR} for $d_c > d_{c,B}$.

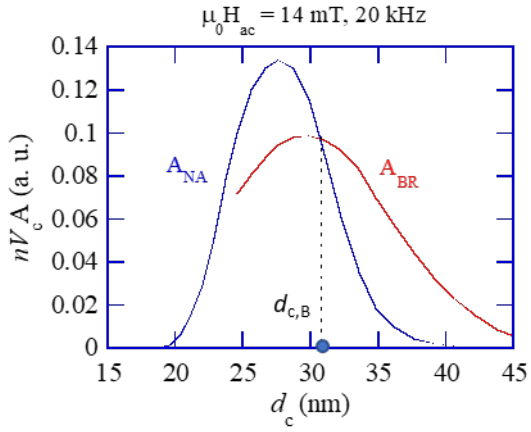

Fig. 4. d_c vs. nV_cA_{NA} and d_c vs. nV_cA_{BR} curves. The curves are calculated for the MS1 sample with d_H = 60 nm when f = 20 kH and $\mu_0 H_{ac}$ = 14 mT.

In Fig. 3, the solid blue lines represent the $<A_W>$ vs. H_{ac} curves calculated from Eq. (19) for the suspended samples. In the calculation, we neglected the d_H distribution in the sample for simplicity. We took d_H as an adjustable parameter and set d_H = 50, 60 and 70 nm for synomag, MS1 and perimag, respectively. The d_H values were consistent with the nominal ones for synomag and MS1, while d_H was smaller than the nominal value for perimag. We obtained good agreement between experiment and analysis for the three samples. These agreements indicate the validity of Eq. (19).

For comparison, the broken lines in Fig. 3 are the $<A_{NA}>$ vs. H_{ac} curves calculated by setting $d_{c,B} = \infty$ in Eq. (19). We note that the difference between $<A_W>$ and $<A_{NA}>$ represents the effect of Brownian relaxation. In Fig. 3(a), the difference between $<A_W>$ and $<A_{NA}>$ is small for the synomag sample, indicating that the effect of Brownian relaxation is negligible. For the MS1 and perimag samples, $<A_W>$ was almost the same as $<A_{NA}>$ for $\mu_0 H_{ac}$ > 16 mT. However, the difference between them increased with decreasing H_{ac} for $\mu_0 H_{ac}$ < 16 mT. These results indicate that the effect of Brownian relaxation is small at high fields but becomes larger at low fields.

We now study the value of $d_{c,B}$ in Eq. (19) that separates the Néel-relaxation-dominant and Brownian-relaxation-dominant MNPs in the sample; $d_{c,B}$ can be calculated from Eqs. (12) and (16) with the condition $A_{BR} = A_{NA}$. We note that $d_{c,B}$ becomes dependent on H_{ac}, indicating that the portion of Néel-relaxation- and Brownian-relaxation-dominant MNPs changes when H_{ac} changes. Fig. 5(a) shows the dependence of $d_{c,B}$ on H_{ac}, whereby $d_{c,B}$ increases with increasing H_{ac}. Because Néel relaxation becomes dominant for MNPs with $d_c < d_{c,B}$, this result indicates that the portion of Néel-

relaxation-dominant MNPs in the sample increases with H_{ac}. The volume fraction of these MNPs, VF_{Neel}, is estimated as

$$VF_{Neel} = \int_0^{d_{c,B}} nV_c \, dd_c \Big/ \int_0^{\infty} nV_c \, dd_c \,. \quad (20)$$

Fig. 5(b) presents the increase in volume fraction with H_{ac}. The volume fraction becomes larger than 90% at high fields. This result means that the AC *M*–*H* curve of the suspended sample is almost dominated by Néel relaxation at high fields. However, the volume fraction decreases with decreasing H_{ac}, corresponding to the increase in Brownian-relaxation-dominant MNPs at low fields. Therefore, the contribution of Brownian relaxation increases at lower fields. From Fig. 5(b), we see that the volume fraction of Brownian-relaxation-dominant MNPs at $\mu_0 H_{ac} = 8$ mT was 30% for MS1 and 17% for synomag. Therefore, the effect of Brownian relaxation is largest for MS1 and smallest for synomag.

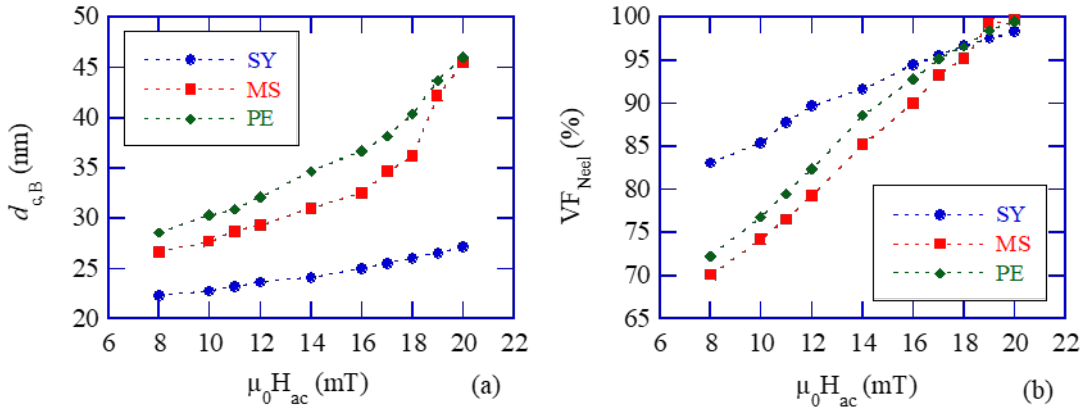

Fig. 5. (a) $d_{c,B}$ vs. H_{ac} curves. (b) Change in volume fraction of Néel-relaxation-dominant MNPs in the three samples when H_{ac} is varied. The broken lines are for the eyes.

3.3. Comparison between immobilized and suspended samples

3.3.1. Hysteresis loss and coercive field

We first compare <*A*> between suspended (water) and immobilized (solid) samples. The ratio $R_{<A>}$ is defined as

$$R_{\langle A \rangle} = \frac{\langle A(\text{water}) \rangle}{\langle A(\text{solid}) \rangle} \,. \quad (21)$$

Fig. 6(a) presents the dependence of $R_{<A>}$ on H_{ac} for the three samples. For $\mu_0 H_{ac} > 16$ mT, the $R_{<A>}$ values for MS1 and perimag were almost the same and were much larger than that for synomag. From Eq. (17), $R_{<A>}$ depends on ξ_{ac} (or m). In Table I, the typical value of m, m_{typ}, is estimated as 1.02, 2.51 and 2.30 aAm^2 for synomag, MS1 and perimag, respectively. Therefore, the small value of $R_{<A>}$

for synomag was caused by the low m_{typ}.

For $\mu_0 H_{ac} < 16$ mT, $R_{<A>}$ increased with decreasing H_{ac}. The increase was largest for MS1 and smallest for synomag. We note that Brownian relaxation is responsible for these properties because the fraction of Brownian-relaxation-dominated MNPs increases with decreasing H_{ac}, and the fraction is smallest for synomag, as shown in Fig. 5(b).

Next, we compare $<H_c>$ between suspended and immobilized samples. The ratio of $<H_c>$ for a suspended sample to the value for an immobilized sample is

$$R_{\langle Hc\rangle} = \frac{\langle H_c(\text{water})\rangle}{\langle H_c(\text{solid})\rangle}. \quad (22)$$

Fig. 6(b) presents the dependence of $R_{<Hc>}$ on H_{ac} for the three samples. The value of $R_{<Hc>}$ was much smaller than $R_{<A>}$. Furthermore, $R_{<Hc>}$ depended weakly on H_{ac}. Therefore, the difference in the coercive field was much smaller between the suspended and immobilized cases than the hysteresis loss.

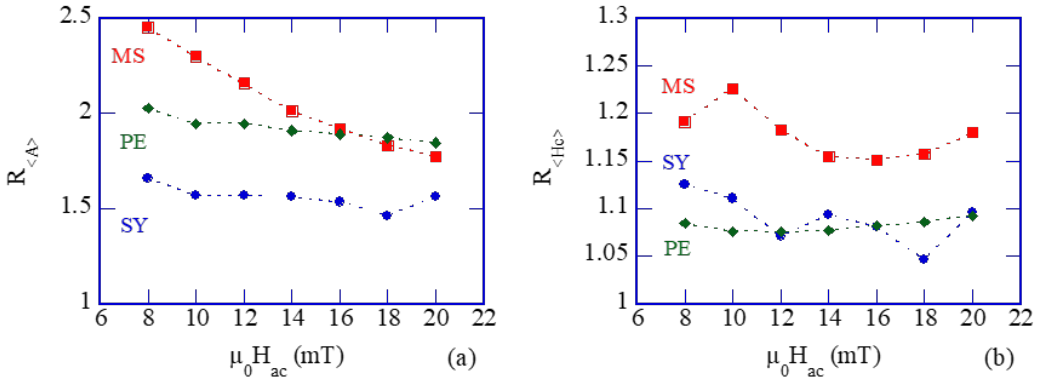

Fig. 6. (a) $R_{<A>}$ vs. H_{ac} and (b) $R_{<Hc>}$ vs. H_{ac} curves for the three MNP samples.

We note that the parameter κ in Eq. (5) satisfies the condition $\kappa > 0.4$ for the present sample parameters and excitation conditions. In our previous paper [38], we studied the dependence of H_c on the easy-axis angle β, and showed that the dependence becomes small for $\kappa > 0.4$. In this case, therefore, $<H_c>$ increases only slightly even when alignment of β occurs in suspended sample. As a result, the difference in $<H_c>$ is small between the suspended and immobilized cases in the present experiment. We note, however, that the dependence of H_c on β becomes stronger with decreasing κ. Therefore, the difference in $<H_c>$ will become large between the suspended and immobilized cases when κ becomes much smaller.

3.3.2. Harmonic signals

Finally, we compare the harmonic signals between suspended and immobilized samples. The amplitude of the harmonic signal, M_i (i = 1, 3, 5…), was obtained by expanding the measured waveform $M(t)$ into a Fourier series. The M_i ratio between the two cases is

$$R_{Mi} = \frac{M_i(\text{water})}{M_i(\text{solid})}, i = 1, 3, 5 \ldots. \quad (23)$$

We studied the 3rd and 5th harmonics as examples. These harmonics are used for biosensing [14, 16, 18]. Fig. 7(a) presents the dependences of R_{M3} on H_{ac} for the three samples. These dependences are similar to the $R_{<A>}$ vs. H_{ac} curves in Fig. 6(a). Specifically, R_{M3} increases in the order synomag, perimag and MS1. For MS1, R_{M3} considerably increases with decreasing H_{ac}. However, R_{M3} is almost independent of H_{ac} for synomag. This difference is due to the fact that the portion of Brownian-relaxation-dominated MNPs was small for the synomag sample.

Fig. 7(b) presents the relationship between R_{M5} and R_{M3}. The relation R_{M5} vs. R_{M3} is almost on the same curve for all three MNP samples. This indicates a strong correlation between R_{M3} and R_{M5} among the three samples, though the physical mechanism for this correlation is not clear at present. The solid line in Fig. 7(b) represents the correlation given by

$$R_{M5} = 0.8R_{M3} + 0.3R_{M3}^2. \quad (24)$$

We note that similar behavior was obtained for the relationship between R_{M7} and R_{M5}. However, the relation R_{M3} vs. R_{M1} was different among samples. It will be our future work to clarify the relationship between harmonies signals.

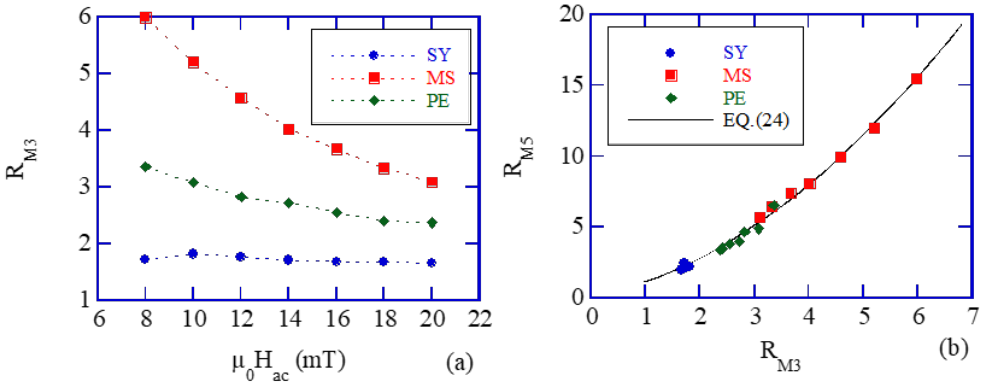

Fig. 7. Relationship (a) between R_{M3} and H_{ac} and (b) between R_{M5} and R_{M3} for the three samples. The broken lines in (a) are for the eyes. The solid line in (b) is calculated using Eq. (24).

4. Discussion

4.1 Condition for the Néel- and Brownian-dominant regions

The AC *M–H* curve of suspended MNPs is affected by both Brownian and Néel relaxations. We will study the condition that determines the dominant relaxation. First, we study $\tau_B(H)$ and $\tau_N(H)$. The

expression for $\tau_B(H)$ is given in Eq. (15). The expression for $\tau_N(H)$ is [39]

$$\tau_N(H) = \frac{\tau_0\sqrt{\pi}}{\sqrt{\sigma}(1-h^2)} \frac{1}{(1+h)\mathrm{e}^{-\sigma(1+h)^2} + (1-h)\mathrm{e}^{-\sigma(1-h)^2}}, \quad (25)$$

where $h = H/H_k$ is the normalized field. In this study, we use Eq. (25) for simplicity, though Eq. (25) is obtained when the easy axis is parallel to the applied field.

Fig. 8(a) shows examples of $\tau_B(H)$ and $\tau_N(H)$. In the calculation, we used the parameters corresponding to the MS1 sample: M_s = 360 kA/m, K = 7.0 kJ/m^3, $\mu_0 H_k$ = 38.9 mT and d_H = 60 nm. The value d_c = 28 nm was chosen because nV_cA has a peak value at approximately d_c = 28 nm for MS1, as shown in Fig. 4. As shown in Fig. 8(a), $\tau_N >> \tau_B$ at low fields. Therefore, Brownian relaxation becomes dominant in the low-field region. However, τ_N rapidly decreases with increasing H, and $\tau_N = \tau_B$ at $H = H_{ac,BR}$; $\mu_0 H_{ac,BR}$ = 10.2 mT for d_c = 28 nm. As a result, $\tau_N << \tau_B$ for $H > H_{ac,BR}$, and Néel relaxation dominates the dynamics of suspended MNPs at high fields.

For comparison, Fig. 8(a) also shows $\tau_N(H)$ calculated for d_c = 25 nm. The value of $H_{ac,BR}$ becomes very small in this case, and Néel relaxation becomes dominant for almost all fields.

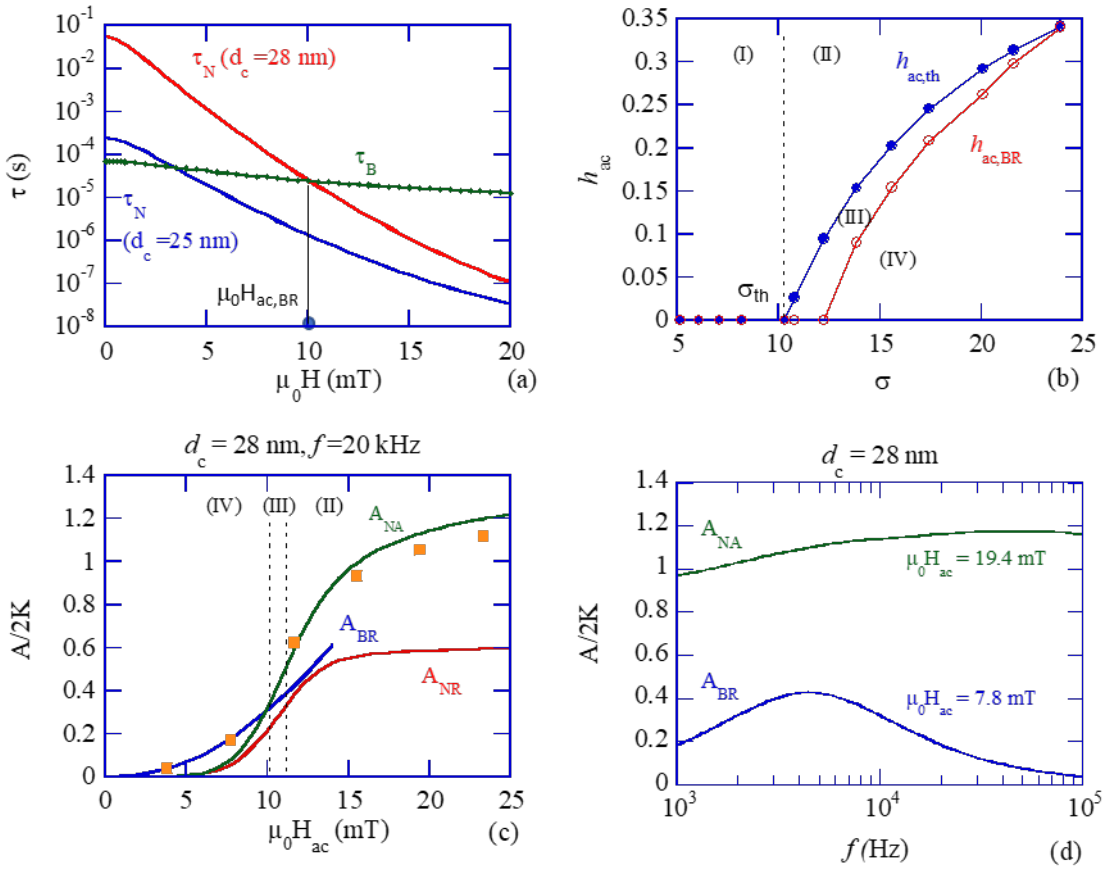

Fig. 8. (a) Field-dependent Brownian relaxation time $\tau_B(H)$ and Néel relaxation time $\tau_N(H)$. (b) Four regions in the σ–h_{ac} plane. The boundary between regions (II) and (III) is determined by $h_{ac,th}$

calculated from Eq. (8). The boundary between regions (III) and (IV) is determined by $h_{ac,BR}$, which satisfies the condition $\tau_N(h_{ac,BR}) = \tau_B(h_{ac,BR})$. (c) $A/(2K)$ vs. H_{ac} curves for $d_c = 28$ nm. Lines show the results for A_{NR}, A_{BR} and A_{NA} calculated using Eqs. (4), (12) and (16), respectively. Symbols represent the simulation results for suspended MNPs. (d) $A/(2K)$ vs. f curves for $d_c = 28$ nm and two values of H_{ac}. For $\mu_0 H_{ac} = 7.8$ mT, line shows A_{BR} calculated using Eq. (12). For $\mu_0 H_{ac} = 19.4$ mT, line shows A_{NA} calculated using Eq. (16).

We now study the condition that determines the dominant relaxation in suspended MNPs using the σ–h_{ac} plane, as shown in Fig. 8(b). The σ–h_{ac} plane is calculated for $f = 20$ kHz and can be divided into four regions. Region (I) is determined by the condition $\sigma < \sigma_{th}$, where σ_{th} in Eq. (10) becomes 10.3 for $f = 20$ kHz. In this region, the condition $2\pi f\tau_N(0) < 1$ is satisfied, and Néel relaxation dominates the MNP dynamics. The hysteresis loss in this region is A_{NR} in Eq. (4). For sufficiently low σ, linear theory can be applied using the AC susceptibility of MNPs [4].

Region (II) is determined by the condition $h_{ac} > h_{ac,th}$, where $h_{ac,th}$ is given in Eq. (8). We note that $h_{ac,th}$ gives the threshold field for the magnetic moment reversal over the anisotropy energy barrier [25, 38]. In this region, the condition $\tau_N(H) < 1/(2\pi ft) << \tau_B(H)$ is satisfied, and Néel relaxation becomes dominant. When the AC field is applied, the magnetic moment changes its polarity by passing the anisotropy energy barrier. Furthermore, the AC field causes successive Brownian (physical) rotation in suspended MNPs, and easy axes are partially aligned along the AC field. The hysteresis loss in this region is A_{NA} in Eq. (16).

Region (IV) is determined by the condition $h_{ac} < h_{ac,BR}$, where $h_{ac,BR}$ is the field satisfying $\tau_N(h_{ac,BR}) = \tau_B(h_{ac,BR})$. In this region, $\tau_B(H) < \tau_N(H)$, and therefore, Brownian relaxation becomes dominant. The hysteresis loss in this region is A_{BR} in Eq. (12). We note that A_{BR} strongly depends on $2\pi f\tau_B(H)$, as shown in Eq. (12). Namely, the effect of Brownian relaxation is largest for $2\pi f\tau_B(\mathrm{H}) \approx 1$, but can be neglected at high frequencies satisfying $2\pi f\tau_B(H) >> 1$.

Region (III) is determined by the condition $h_{ac,BR} < h_{ac} < h_{ac,th}$. In this region, both Brownian and Néel relaxations affect the AC M–H curve of the suspended sample in a complicated way.

We note that the range of h_{ac} for regions (II) and (IV) changes with σ, as shown in Fig. 8(b). As σ decreases, the range of h_{ac} increases in region (II) and decreases in region (IV). This means that the effect of Brownian relaxation decreases for MNPs with lower σ (or d_c). We also note that $h_{ac,th}$ in Fig. 8(b) increases with increasing f, as can be seen from Eq. (8). This means that region (II) moves to a higher h_{ac} value for higher f. However, $h_{ac,BR}$ is independent of f, and region (IV) does not change when f is changed.

We now show the A vs. H_{ac} curve calculated for each region. The lines in Fig. 8(c) represent the results calculated for parameters $M_s = 360$ kA/m, $K = 7.0$ kJ/m^3, $\mu_0 H_k = 38.9$ mT, $d_c = 28$ nm and d_H

= 60 nm. The results for A_{NR}, A_{BR} and A_{NA} are calculated using Eqs. (4), (12), and (16), respectively. From Fig. 8(b), we obtained $\mu_0 H_{ac,BR}$ = 10.2 mT and $\mu_0 H_{ac,th}$ = 11.4 mT for d_c = 28 nm (σ=19.4). Using these values, the field H_{ac} can be divided into regions (IV), (III) and (II), as shown in Fig. 8(c). In region (IV), Brownian relaxation is dominant and A is given by A_{BR}. In region (II), Néel relaxation is dominant and A is given by A_{NA}. In Region (III), we take the larger of A_{BR} and A_{NA} as the hysteresis loss. We note that region (I) does not exist because $\sigma > \sigma_{th}$ in this case.

For comparison, the AC M–H curve of suspended MNPs was numerically simulated for d_c = 28 nm and f = 20 kHz. The symbols in Fig. 8(c) represent the simulated $A/(2K)$ vs. H_{ac} curves. In the simulation, both the dynamics of the magnetic moment $\boldsymbol{m}$ and the unit vector along the easy axis, $\boldsymbol{n}$, were solved simultaneously via the stochastic Landau–Lifshitz–Gilbert equation and an equation from *Usov et al.* [22, 25]. We obtained good agreement between simulation and analysis, indicating the validity of the analysis.

Finally, we discuss the frequency dependence of A_{BR} in region (IV) and A_{NA} in region (II). As shown in Fig. 8(c), Brownian relaxation is dominant at $\mu_0 H_{ac}$ = 7.8 mT (h_{ac} = 0.2), and A is given by A_{BR} in Eq. (12). The blue line in Fig. 8(d) shows the frequency dependence of A_{BR} calculated for $\mu_0 H_{ac}$ = 7.8 mT. As shown, A_{BR} strongly depends on f. Namely, A_{BR} becomes large for $2\pi f \tau_B(H) \approx 1$ ($f \approx 4.5$ kHz), but becomes very small at high frequencies satisfying $2\pi f \tau_B(H) >> 1$. On the other hand, Néel relaxation is dominant at $\mu_0 H_{ac}$ = 19.4 mT (h_{ac} = 0.5) as shown in Fig. 8(c), and A is given by A_{NA} in Eq. (16). The green line in Fig. 8(d) shows the frequency dependence of A_{NA} calculated for $\mu_0 H_{ac}$ = 19.4 mT. As shown, frequency dependence of A_{NA} is very weak. Therefore, frequency dependence is very different between A_{BR} and A_{NA}.

4.2. Degree of easy axis alignment

As shown in Fig. 3, hysteresis loss increased owing to easy axis alignment in the suspended sample when H_{ac} was high. We will discuss the degree of easy axis alignment using the $\langle A \rangle$ vs. H_{ac} curve. Fig. 9(a) presents the measured $\langle A \rangle$ vs. H_{ac} curve, where the vertical axis is normalized by $2K$ and the horizontal axis is normalized by H_k. The open and closed symbols are the results for the immobilized and suspended cases, respectively. In the immobilized case, the $\langle A \rangle/(2K)$ vs. h_{ac} curves become similar among the three MNP samples. In the suspended case, MS1 and perimag have similar $\langle A \rangle/(2K)$ vs. h_{ac} curves, while $\langle A \rangle/(2K)$ is smaller for synomag.

The degree of easy axis alignment can be expressed using the mean orientation of the easy axes through $\langle \cos\beta \rangle$, where β is the easy axis angle, and $\langle \quad \rangle$ means the average over time and the MNP ensemble [20, 22, 38]. When easy axes are aligned, β becomes small and $\langle \cos\beta \rangle$ becomes large. We expect the AC M–H curve to depend on $\langle \cos\beta \rangle H_{ac}$. This is because the AC M–H curve is determined by the distribution of β, and its distribution function, $W_{EA}(\beta)$, is determined by the value of $H_{ac}\cos\beta$ [25, 38]. Therefore, we define the effective field

$$h_{ac,eff} = \begin{cases} h_{ac} & \text{for the immobilized case,} \\ a h_{ac} & \text{for the suspended case ,} \end{cases} \quad (26)$$

where a represents the increase in $\langle \cos\beta \rangle$ caused by the easy axis alignment in a suspended sample.

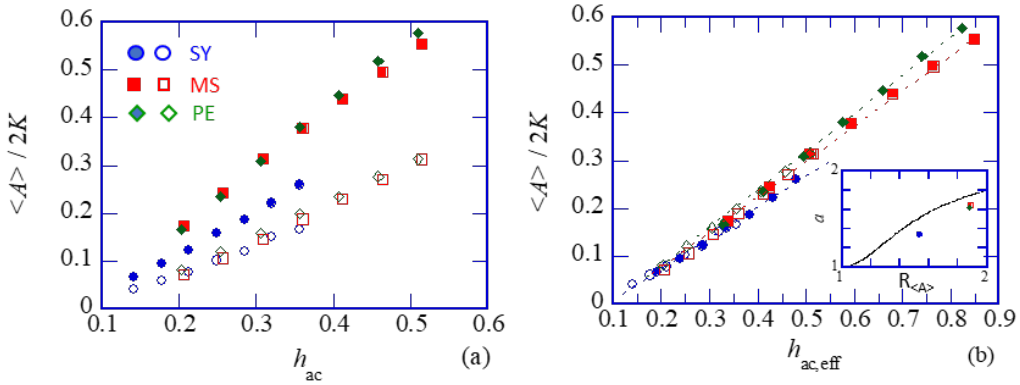

Fig. 9. (a) $\langle A \rangle/(2K)$ vs. h_{ac} relations. Open and closed symbols represent the results for immobilized and suspended cases, respectively. (b) $\langle A \rangle/(2K)$ vs. $h_{ac,eff}$ relations. The value of $h_{ac,eff}$ was calculated from Eq. (26). Broken lines are for eyes. The inset shows the relation between $a = 2\langle \cos\beta \rangle$ and $R_{\langle A \rangle}$.

The $\langle A \rangle/(2K)$ vs. h_{ac} relations in Fig. 9(a) were replotted as the $\langle A \rangle/(2K)$ vs. $h_{ac,eff}$ relations using Eq. (26). The results are shown in Fig. 9(b). To calculate Eq. (26), we used a = 1.35, 1.65 and 1.62 for synomag, MS1 and perimag, respectively. The value of a for each MNP sample was determined so that the $\langle A \rangle/(2K)$ vs. $h_{ac,eff}$ relations for both immobilized and suspended cases would fall on the same curve, as shown by the broken lines in Fig. 9(b).

We note that a in Eq. (26) is the ratio of $\langle \cos\beta \rangle$ between immobilized and suspended cases. It has been shown that $\langle \cos\beta \rangle = 0.5$ (or effective angle β = 60 deg) for the immobilized case with randomly oriented easy axes [22, 38]. Therefore, a is given by $a = 2\langle \cos\beta \rangle$. Using the obtained value of a, we can estimate $\langle \cos\beta \rangle = 0.675, 0.825$ and 0.810 (or β = 48, 34 and 36 deg) for synomag, MS1 and perimag, respectively. These results indicate that the degree of easy axis alignment is smallest for synomag. However, the degree of alignment is almost the same for MS1 and perimag.

We also study the relationship between $\langle \cos\beta \rangle$ and $R_{\langle A \rangle}$ in Fig. 6(a). The symbols in the inset of Fig. 9(b) show the relationship between $R_{\langle A \rangle}$ at $\mu_0 H_{ac}$ = 20 mT and $a = 2\langle \cos\beta \rangle$ for the three MNP samples. The solid line is the analytical result calculated as follows. The expression for R_A is given in Eq. (17) for MNPs with d_c (or ξ_{eff}), and the following expression for $\langle \cos\beta \rangle$ is obtained [38]:

$$\langle \cos\beta \rangle = 1 + \frac{1}{\xi_{eff}} \left(\frac{1 - \cosh\xi_{eff}}{\sinh\xi_{eff}} \right). \quad (27)$$

Combining Eqs. (17) and (27), we obtain the relationship between R_A and $a = 2\langle \cos\beta \rangle$, which is shown by the solid line in the inset of Fig. 9(b). The analytical result is consistent with the experimental

one, though the core size distribution is not taken into account in the analysis.

Finally, we note that the effect of the magnetic dipole–dipole interaction between MNPs is neglected in the present analysis. In our experiment, sample contained 150 μg-Fe in 150 μL sample volume. If we assume that MNPs consist of Fe_3O_4, volume concentration of MNPs becomes as low as c = 0.027 % for the present samples. Form this concentration, we can estimate that the mean distance between particles is about 10 times larger than the diameter of particle. Therefore, dipole–dipole interaction will be small in the present experiment. However, because the dipole–dipole interaction increases with increasing MNP concentration, it is necessary to take account of this effect when the MNP density is much increased [40-42]. We also note that the hysteresis loss can be increased when linear chains of MNP are formed [42, 43].

5. Conclusion

We studied the effect of Néel and Brownian relaxation on the AC M–H curve of suspended MNP samples. First, the $\langle A \rangle$ vs. H_{ac} curves were measured for suspended and immobilized cases using three commercial MNP samples. The experimental results can be quantitatively explained with the previously obtained analytical results when the core size distribution in a sample is taken into account. We showed that Néel-relaxation- and Brownian-relaxation-dominant MNPs coexist in each sample, and that the portion of each changes when H_{ac} changes. At high fields, almost all MNPs became Néel-relaxation-dominant, and easy axis alignment caused by the AC field increased the hysteresis loss for a suspended sample. The portion of Brownian-relaxation-dominant MNPs increased with decreasing H_{ac}, and the Brownian relaxation gave additional loss at low fields. We can use the four regions in the σ–h_{ac} plane in Fig. 8(b) to determine the dominant relaxation mechanism in a suspended sample. We also clarified the difference in harmonic signals between suspended and immobilized samples.

CRediT authorship contribution statement

Keiji Enpuku: Data analysis, Writing - Original draft preparation. **Shuya Yamamura**: Experiment. **Takashi Yoshida**: Numerical simulation, Supervision.

Declaration of competing interest

The authors declare that they have no known competing financial interests or personal relationships that could have appeared to influence the work reported in this paper.

Acknowledgements

This work was supported in part by the Japan Society for the Promotion of Science (JSPS) KAKENHI (Grant Numbers JP20H05652 and JP21H01343).

Appendix A: Estimation of core size distribution

The DC *M–H* curve of a suspended sample can be expressed as

$$M_{dc} = M_s \int_0^\infty n(d_c) V_c L(\xi_{dc}) dd_c\,, \qquad (A1)$$

where L is the Langevin function given by

$$L(\xi_{dc}) = \coth(\xi_{dc}) - \frac{1}{\xi_{dc}} \quad (A2)$$

with $\xi_{dc} = \mu_0 M_s V_c H_{dc}/(k_B T)$.

The d_c vs. $n(d_c)V_c$ curve was obtained by numerically solving the inverse problem in Eq. (A1) using the nonlinear non-negative least squares (NNLS) method [34].

We also note that the Langevin function can be approximated as $L(\xi_{dc}) = 1 - 1/\xi_{dc}$ for $\xi_{dc} > 3$. In this high field region, Eq. (A1) can be expressed as

$$M_{dc} = M_s - \frac{k_B T}{\mu_0 H_{dc}} \int_0^\infty n(d_c) dd_c \; for\; \xi_{dc} > 3. \quad (A3)$$

Therefore, linear relationship can be obtained between M_{dc} and $1/H_{dc}$ at high fields satisfying the condition $\xi_{dc} > 3$. We note that the M_s value can be estimated by extrapolating the linear M_{dc} vs $1/H_{dc}$ relation to $1/H_{dc} = 0$ [33].

Appendix B: Expression for H_c for the AC M–H curve

For immobilized MNPs with core diameter d_c and randomly oriented easy axes, the expression for coercive field H_c is empirically obtained as [35]

$$H_c(d_c) = \begin{cases} 0.48 H_k (1 - \kappa^{0.88}) \times g_c \;\; \text{for } \kappa < 0.66, \\ 0.48 H_k \exp\left\{ -\left(\frac{\kappa}{0.61} \right)^{2.1} \right\} \times g_c \;\; \text{for } \kappa > 0.66, \end{cases} \quad (B1)$$

with

$$g_c = \frac{\exp\left(\frac{h_{ac} - h_{1c}}{\Delta h}\right)}{1 + \exp\left(\frac{h_{ac} - h_{1c}}{\Delta h}\right)}, \qquad (B2)$$

$$h_{1c} = 1.19\left(h_{ac,th}\right)^2 + 0.346 h_{ac,th} + 0.037 \quad (B3)$$

where $h_{ac,th}$ and Δh are given in Eqs. (8) and (9), respectively.

When d_c is distributed in a sample, the coercive field $\langle H_c \rangle$ of the sample is approximately given by the volume-weighted average of H_c of each MNP:

$$\langle H_c \rangle = \frac{1}{\int_{d_{c,min}}^{\infty} nV_c \, dd_c} \int_{d_{c,min}}^{\infty} nV_c \, H_c(d_c) dd_c, \qquad (B4)$$

where $H_c(d_c)$ and nV_c are given in Eq. (B1) and Fig. 1, respectively. We note that the present sample consists of elementary particles and agglomerates, as shown in Fig. 1. In Eq. (B4), the integral is performed from $d_c = d_{c,min}$ to neglect elementary particles because they do not contribute to H_c near room temperature owing to their very small σ values. We tentatively set $d_{c,\,min} = 10$ nm from Fig. 1 for all samples.

References

1. D. Ortega and Q. A. Pankhurst, Magnetic hyperthermia, in Nanoscience: Volume 1: Nanostructures through Chemistry, P. O'Brien, Editor. (2013), Royal Society of Chemistry: Cambridge. p. 60-88. DOI: 10.1039/9781849734844-00060
2. D. Chang, M. Lim, Jeroen A. C. M. Goos, R. Qiao, Yun Yee Ng, F. M. Mansfeld, M. Jackson, T. P. Davis and M. Kavallaris, "Biologically targeted magnetic hyperthermia: potential and limitations", *Front. Pharmacol*., **9,** 83 (2018); https://doi.org/10.3389/fphar.2018.00831
3. J. Carrey, B. Mehdaoui, and M. Respaud, "Simple models for dynamic hysteresis loop calculations of magnetic single-domain nanoparticles: Application to magnetic hyperthermia optimization", *J. Appl. Phys.* **109**, 083921 (2011); https://doi.org/10.1063/1.3551582
4. G. Vallejo-Fernandez, O. Whear, A. G. Roca, S. Hussain, J. Timmis, V. Patel and K. O'Grady, "Mechanisms of hyperthermia in magnetic nanoparticles", *J. Phys. D: Appl. Phys.* **46,** 312001 (2013); https://doi.org/10.1088/0022-3727/46/31/312001
5. S. Ruta, R. Chantrell, and O. Hovorka, "Unified model of hyperthermia via hysteresis heating in systems of interacting magnetic nanoparticles", *Sci Rep* **5**, 9090 (2015). https://doi.org/10.1038/srep09090
6. M. Coïsson, G. Barrera, F. Celegato, L. Martino, S. N. Kane, S. Raghuvanshi, F. Vinai, and P. Tiberto, "Hysteresis losses and specific absorption rate measurements in magnetic nanoparticles for hyperthermia applications", *Biochimica et Biophysica Acta (BBA) - General Subjects*, **1861**, 1545-1558 (2017). https://doi.org/10.1016/j.bbagen.2016.12.006.
7. I. Morales, R. Costo, N. Mille, G.B. Da Silva, J. Carrey, A. Hernando, P. De la Presa, "High frequency hysteresis losses on γ-Fe_2O_3 and Fe_3O_4: susceptibility as a magnetic stamp for chain formation", *Nanomaterials* **8**, 970 (2018). https://doi.org/10.3390/nano8120970
8. S. Ota, SB. Trisnanto, S. Takeuchi, J. Wu, Y. Cheng, and Y. Takemura, "Quantitation method of loss powers using commercial magnetic nanoparticles based on superparamagnetic behavior influenced by anisotropy for hyperthermia", *J. Magn. Magn. Mater*. **538,** 168313 (2021). https://doi.org/10.1016/j.jmmm.2021.168313
9. X. Yu, S. Gao, D. Wu, Z. Li, Y. Mi, T. Yang, F. Sun, L. Wang, R. Liu, S. He, Q. Ge, Y. Lv, A. Xu, H. Zeng, "Bone tumor suppression in rabbits by hyperthermia below the clinical safety limit using aligned magnetic bone cement", *Small* **18**, 2104626 (2022). https://doi.org/10.1002/smll.202104626
10. L. C. Wu, Y. Zhang, G. Steinberg, H. Qu, S. Huang, M. Cheng, T. Bliss, F. Du, J. Rao, G. Song, L. Pisani, T. Doyle, S. Conolly, K. Krishnan, G. Grant and M. Wintermark, "A review of magnetic particle imaging and perspectives on neuroimaging", *American Journal of Neuroradiology,* **40**, 206-212 (2019); DOI: https://doi.org/10.3174/ajnr.A5896
11. M. Graeser, F. Thieben, P. Szwargulski, F. Werner, N. Gdaniec, M. Boberg, F. Griese, M. Möddel,

P. Ludewig, D. van de Ven, O. M. Weber, O. Woywode, B. Gleich, and T. Knopp “Human-sized magnetic particle imaging for brain applications”, *Nat Commun* **10**, 1936 (2019). https://doi.org/10.1038/s41467-019-09704-x

12. L. R. Croft, P. W. Goodwill, J. J. Konkle, H. Arami, D. A. Price, A. X. Li, E. U. Saritas, S. M. Conolly, “Low drive field amplitude for improved image resolution in magnetic particle imaging”, *Medical physics*, **43**, 424 (2016). https://doi.org/10.1118/1.4938097
13. H. Paysen, N. Loewa, A. Stach, J. Wells, O. Kosch, S. Twamley, M. R. Makowski, T. Schaeffter, A. Ludwig, F. Wiekhorst, “Cellular uptake of magnetic nanoparticles imaged and quantified by magnetic particle imaging”, *Sci Rep* **10,** 1922 (2020). https://doi.org/10.1038/s41598-020-58853-3
14. K. Wu, D. Su, R. Saha, J. Liu, V. K. Chugh, and Jian-Ping Wang, "Magnetic particle spectroscopy: A short review of applications using magnetic nanoparticles", *ACS Appl. Nano Mater.* **3**, 4972–4989 (2020). https://doi.org/10.1021/acsanm.0c00890
15. J. Fock, M. Parmvi, M. Strömberg, P. Svedlindh, M. Donolato, M. F. Hansen, “Comparison of optomagnetic and AC susceptibility readouts in a magnetic nanoparticle agglutination assay for detection of C-reactive protein”, *Biosensors and Bioelectronics*, **88**, 94-100 (2017). https://doi.org/10.1016/j.bios.2016.07.088
16. K. Enpuku1, M. Shibakura, Y. Arao, T. Mizoguchi, A. Kandori, M. Hara and K. Tsukada, "Wash-free detection of C-reactive protein based on third-harmonic signal measurement of magnetic markers", *Jpn. J. Appl. Phys.* **57**, 090309 (2018). https://doi.org/10.7567/JJAP.57.090309
17. J.-J. Chieh, W.-C. Wei, S.-H. Liao, H.-H. Chen, Y.-F. Lee, F.-C. Lin, M.-H. Chiang, M.-J. Chiu, H.-E. Horng, and S.-Y. Yang, “Eight-channel AC magnetosusceptometer of magnetic nanoparticles for high-throughput and ultra-high-sensitivity immunoassay”, *Sensors* **18**, 1043 (2018). https://doi.org/10.3390/s18041043
18. J. Zhong, E. L. Rösch, T. Viereck, M. Schilling, and F. Ludwig, “Toward rapid and sensitive detection of SARS-CoV-2 with functionalized magnetic nanoparticles”, *ACS Sens.* **6**, 976–984 (2021). https://doi.org/10.1021/acssensors.0c02160
19. T. Yoshida1, K. Ogawa1, K. Enpuku, N. Usuki, and H. Kanzaki, “AC susceptibility of magnetic fluid in nonlinear Brownian relaxation region: Experiment and comparison with numerical simulation”, *Jpn. J. Appl. Phys*. **49**, 053001 (2010). https://doi.org/10.1143/JJAP.49.053001
20. H. Mamiya, and B. Jeyadevan, “Hyperthermic effects of dissipative structures of magnetic nanoparticles in large alternating magnetic fields”, *Sci Rep* **1**, 157 (2011). DOI: 10.1038/srep00157
21. S. A. Shah, D. B. Reeves, R. M. Ferguson, J. B. Weaver, and K. M. Krishnan, "Mixed Brownian alignment and Néel rotations in superparamagnetic iron oxide nanoparticle suspensions driven by an ac field”, *Phys. Rev.* **B 92**, 094438 (2015). https://doi.org/10.1103/PhysRevB.92.094438

22. T. Yoshida, S. Bai, A. Hirokawa, K. Tanabe, K. Enpuku, “Effect of viscosity on harmonic signals from magnetic fluid”, *J. Magn. Magn. Mater.*, **380**, 105-110 (2015). https://doi.org/10.1016/j.jmmm.2014.10.044
23. M. Suwa, A. Uotani, and S. Tsukahara, “Magnetic and viscous modes for physical rotation of magnetic nanoparticles in liquid under oscillating magnetic field”, *Appl. Phys. Lett.* **116**, 262403 (2020); https://doi.org/10.1063/5.0010095
24. Ahmed L. Elrefai, K. Enpuku, and T. Yoshida, “Effect of easy axis alignment on dynamic magnetization of immobilized and suspended magnetic nanoparticles”, *J. Appl. Phys*. **129**, 093905 (2021); https://doi.org/10.1063/5.0041215
25. K. Enpuku, Ahmed L. Elrefai, J. Gotou, S. Yamamura, T. Sasayama and T. Yoshida, “Difference in AC magnetization between suspended and immobilized magnetic nanoparticles in Néel-relaxation dominant case: Effect of easy axis alignment in suspended nanoparticles”, *J. Appl. Phys.* **130**, 113903 (2021); https://doi.org/10.1063/5.0056481
26. D.-X. Chen, N. Sun, and H.-C. Gu, “Size analysis of carboxydextran coated superparamagnetic iron oxide particles used as contrast agents of magnetic resonance imaging”, *J. Appl. Phys*. **106**, 063906 (2009). https://doi.org/10.1063/1.3211307
27. K. Enpuku, Ahmed L. Elrefai, T. Yoshida, T. Kahmann, J. Zhong, T. Viereck, and F. Ludwig, “Estimation of the effective magnetic anisotropy constant of multi-core based magnetic nanoparticles from the temperature dependence of the coercive field”, *J. Appl. Phys*. **127**, 133903 (2020); https://doi.org/10.1063/1.5144713
28. Technical data sheets for synomag and perimag are given in https://micromod.de/wp-content/uploads/datasheets/104-02-501_tds_en.pdf and https://micromod.de/wp-content/uploads/datasheets/102-02-132_tds_en.pdf, respectively.
29. K. Riahi, M.M. van de Loosdrecht, L. Alic, and B. ten Haken, “Assessment of differential magnetic susceptibility in nanoparticles: Effects of changes in viscosity and immobilization”, *J. Magn. Magn. Mater.* **514**, 167238 (2020); https://doi.org/10.1016/j.jmmm.2020.167238.
30. T. Yoshida, N. B. Othman, and K. Enpuku, “Characterization of magnetically fractionated magnetic nanoparticles for magnetic particle imaging”, *J. Appl. Phys.* **114**, 173908 (2013); https://doi.org/10.1063/1.4829484
31. ZW. Tay, P. Chandrasekharan, XY. Zhou, E. Yu, B. Zheng, and S.Conolly, “In vivo tracking and quantification of inhaled aerosol using magnetic particle imaging towards inhaled therapeutic monitoring”, *Theranostics* **8**, 3676-3687 (2018); doi: 10.7150/thno.26608.
32. T. Sasayama, T. Yoshida, K. Tanabe, N. Tsujimura and K. Enpuku, "Hysteresis Loss of Fractionated Magnetic Nanoparticles for Hyperthermia Application," *IEEE Trans. Magn.* **51**, 5101504 (2015) doi: 10.1109/TMAG.2015.2438080.
33. R. Chantrell, J. Popplewell and S. Charles, "Measurements of particle size distribution parameters

in ferrofluids," *IEEE Trans. Magn.*, **14**, 975-977 (1978), doi: 10.1109/TMAG.1978.1059918.

34. Ahmed L. Elrefai, T. Sasayama, T. Yoshida, and K. Enpuku, "Magnetic core-size distribution of magnetic nanoparticles estimated from magnetization, AC susceptibility, and relaxation measurements", *IEEE Trans. Magn.* **53**, 8204605 (2017) DOI: 10.1109/TMAG.2017.2700480
35. K. Enpuku, S. Draack, F. Ludwig, and T. Yoshida, "Evaluation of effective magnetic anisotropy constant of magnetic nanoparticles from coercive field of AC magnetization curve", *J. Appl. Phys.* **130**, 183901 (2021); https://doi.org/10.1063/5.0070321
36. K. Enpuku and T. Yoshida, "Expression for hysteresis loss of immobilized magnetic nanoparticles in a wide range of particle parameters and excitation conditions: Parameter optimization for hyperthermia application", *AIP Advances* **11**, 125123 (2021); https://doi.org/10.1063/5.0076534
37. J. Dieckhoff, D. Eberbeck, M. Schilling, F. Ludwig, "Magnetic-field dependence of Brownian and Néel relaxation times", *J. Appl. Phys.* **119**, 043903 (2016). https://doi.org/10.1063/1.4940724
38. K. Enpuku and T. Yoshida, "Dependence of hysteresis loss of immobilized magnetic nanoparticles on the easy-axis angle: Effect of easy-axis alignment", *AIP Advances* **12**, 055211 (2022); https://doi.org/10.1063/5.0090915
39. W.T. Coffey, P.J. Cregg, Y.U.P. Kalmykov, "On the Theory of Debye and Néel Relaxation of Single Domain Ferromagnetic Particles", in: *Adv. Chem. Phys*., Wiley-Blackwell, 2007: pp. 263–464. doi:10.1002/9780470141410.ch5.
40. S. Mørup, M. F. Hansen, and C. Frandsen, "Magnetic interactions between nanoparticles" *Beilstein J. Nanotechnol.* **1**, 182 (2010). https://doi.org/10.3762/bjnano.1.22
41. Jw. Kim, J. Wang, H. Kim and S. Bae, "Concentration-dependent oscillation of specific loss power in magnetic nanofluid hyperthermia", *Sci Rep* **11**, 733 (2021). https://doi-org.anywhere.lib.kyushu-u.ac.jp/10.1038/s41598-020-79871-1
42. LC. Branquinho, MS. Carrião, AS. Costa, N. Zufelato, MH. Sousa, R. Miotto, R. Ivkov, and AF. Bakuzis, "Effect of magnetic dipolar interactions on nanoparticle heating efficiency: Implications for cancer hyperthermia", *Sci Rep* **3**, 2887(2013). https://doi.org/10.1038/srep02887
43. D. P. Valdés, E. Lima,, Jr., R. D. Zysler, G. F. Goya, and E. D. Biasi, "Role of anisotropy, frequency, and interactions in magnetic hyperthermia applications: Noninteracting nanoparticles and linear chain arrangements", *Phys. Rev. Applied* **15,** 044005 (2021). https://doi.org/10.1103/PhysRevApplied.15.044005